

Wake-induced variations in noise levels and amplitude modulation for two interacting wind turbines

Jules Colas,¹ Ariane Emmanuelli,¹ Didier Dragna,^{1, a} and Richard J.A.M. Stevens²

¹*Ecole Centrale de Lyon, CNRS, Université Claude Bernard Lyon 1, INSA Lyon, LMFA, UMR5509, 69130, Ecully, France*

²*Physics of Fluids Group, Max Planck Center Twente for Complex Fluid Dynamics, J. M. Burgers Center for Fluid Dynamics, University of Twente, P. O. Box 217, 7500 AE Enschede, The Netherlands*

The influence of turbine–turbine interactions on sound propagation is investigated using numerical simulations. Three configurations are examined: turbines aligned downstream of each other, placed side by side, and arranged in a staggered pattern. The simulation framework combines large-eddy simulations for aerodynamic interactions, an aeroacoustic source model to simulate turbine sound emission, and parabolic equation methods for sound propagation. When a second turbine is positioned directly downstream, wake-induced flow focusing enhances sound pressure levels (SPL) and amplitude modulation (AM) by several decibels downwind. In side-by-side and staggered configurations, SPL increases are limited (< 2 dBA), and AM is generally reduced due to spatial averaging. Distinct AM patterns emerge in regions where acoustic contributions from both turbines are comparable. For nearly identical rotor speeds, AM is strongly affected by the angular offset between rotors. When rotor speeds differ slightly, beating effects occur, resulting in intermittent AM. These findings highlight the sensitivity of AM to rotor dynamics, a key factor influencing sound perception, with implications for environmental impact and turbine siting.

^adidier.dragna@ec-lyon.fr

I. INTRODUCTION

Noise generated by wind turbines is a critical factor influencing public acceptance of wind energy. It has also an economical cost, as curtailment plans for noise mitigation result in loss of electrical production. However, predicting noise production and propagation from wind turbines remains a challenge. It requires a detailed description of the flow around the turbines, the noise sources themselves, and the propagation of sound through the atmosphere.

During the past decade, significant progress has been made in these various aspects. Flow fields obtained from computational fluid dynamics simulations are now widely incorporated into propagation simulations ([Barlas *et al.*, 2017a](#); [Heimann *et al.*, 2018](#)), providing more realistic representations than analytical profiles. Advanced source models, including extended and moving sources, have also been developed ([Bresciani *et al.*, 2024](#); [Shen *et al.*, 2022](#); [Tian and Cotté, 2016](#)). In parallel, several propagation models have been introduced. Wave-based approaches, based on either the parabolic equation ([Kayser *et al.*, 2020](#); [Lee *et al.*, 2016](#); [Nyborg *et al.*, 2023a](#)) or the linearized Euler equations ([Colas *et al.*, 2024](#)) are the state of the art for wind turbine noise studies. While they have been restricted to two-dimensional configurations, first simulations using three-dimensional parabolic equations have been recently reported ([Bommidala *et al.*, 2025](#)), although limited to low frequencies.

Most applications in the literature have been devoted to an isolated wind turbine and few studies have considered noise propagation from multiple turbines. So far, the effects of successive turbine wakes for a row of aligned wind turbines have been examined by [Sun *et al.* \(2018\)](#) using a single point source at the hub. [Shen *et al.* \(2019\)](#) have illustrated the overall

Noise levels and amplitude modulation for two interacting wind turbines sound pressure level for a wind farm of 25 turbines in real complex terrain. Optimization of a wind farm layout including a noise criterion has been investigated by Nyborg *et al.* (2023b). Despite these studies, sound propagation from multiple turbines has not been systematically examined.

In this study, we address this gap by considering noise propagation from a pair of wind turbines as a canonical case for multiple wind turbines. Four configurations are considered: a single isolated turbine as a reference, and a pair of turbines arranged either side by side, one behind the other, or in a staggered layout.

The paper is organized as follows. In Sec. II, the four configurations and the numerical methods are introduced. Sec. III presents the mean flow, the source characteristics, and the propagation effects. Sec. IV details the average sound pressure level and the amplitude modulation around the wind turbine pair. Finally, concluding remarks are given in Sec. V.

II. SCENARIO AND METHODS

A. Configurations

Four configurations are considered, as illustrated in Fig. 1. First, a baseline case with a single turbine is simulated (case B). It is then compared with three layouts of wind turbine pairs: column (case C), line (case L) and staggered (case S) layouts. The turbines are spaced out by four rotor diameters (480 m) in the x - and y -directions. In the following, index 1 refers to the upstream turbine and index 2 to the downstream turbine, as depicted in Fig. 1.

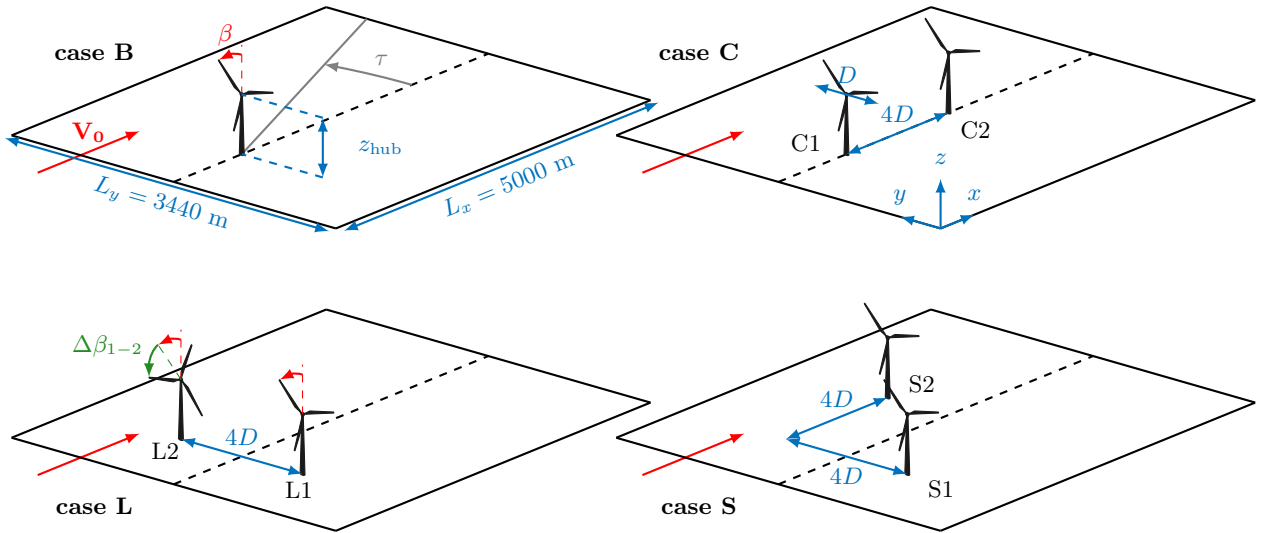


FIG. 1. Sketch of the four configurations.

The turbines are all identical and have a hub height $z_{\text{hub}} = 90$ m. The geometry of the blades is that proposed in [Tian and Cotté \(2016\)](#), except that the rotor diameter is scaled up to $D = 120$ m so that the dimensions of the wind turbines correspond to those of the 5 MW NREL wind turbine ([Jonkman *et al.*, 2009](#)).

A stable atmospheric boundary layer (ABL) is considered because it is generally considered the worst-case scenario for wind turbine sound propagation ([Barlas *et al.*, 2018](#); [Heimann and Englberger, 2018](#)). The stable atmosphere is simulated with a cooling rate equal to -0.2 K h^{-1} , a roughness length equal to 0.1 m and a friction velocity of 0.6 m s^{-1} to obtain a wind speed at hub height equal to 11.4 m s^{-1} .

B. Methods

Wind turbine noise propagation requires three elements: a description of the atmospheric flow, a model for the wind turbine source, and a model for sound propagation.

1. *Atmospheric flow*

The atmospheric flow is obtained using large-eddy simulations (LES) (Gadde *et al.*, 2021; Stevens *et al.*, 2014). An actuator disk approach is used to model the wind turbine (Stevens *et al.*, 2018). The LES is run until a statistical stationary solution is obtained; the mean flow fields are then determined by time averaging the instantaneous fields over four hours. For simplicity, while the LES provide spatially-varying temperature fields, we use a constant temperature and sound speed in the following.

2. *Source model*

The source model is that developed by Tian and Cotté (2016). Each blade is split into segments with a sufficiently large span compared to its cord, along which the geometrical and flow properties are assumed to be constant. Amiet's theory is then applied to determine the turbulent inflow noise (TIN) and the trailing edge noise (TEN) due to each segment. TIN requires a model for the spectrum of the velocity fluctuations in the incoming flow for which the Kolmogorov spectrum is used as in Mascarenhas *et al.* (2022). TEN necessitates a model for the spectrum of wall pressure fluctuations for which the model proposed by Lee and Shum (2019) is chosen, using the boundary layer properties at the trailing edge determined with

XFOIL (Drela, 1989). In addition, the LES data in the rotor plane are used to specify the mean flow velocity and the turbulent dissipation rate, which are required for TIN and TEN computations. Finally, the source model provides the sound pressure level in the free field, denoted $\text{SPL}_{\text{ff}}(m, \beta, f)$, for each blade segment indexed by m as a function of the frequency f and the rotor angle β .

As the flow in the rotor plane is different for each turbine, it is also necessary to specify a control law that relates the rotational speed of the rotor Ω to the impinging flow. For that, we use the relation that gives Ω from the wind speed at the hub u_{hub} for the NREL wind turbine (see Fig. 9-1 in Jonkman *et al.* (2009)). The corresponding values in the cut-in, rated and cut-out conditions are indicated in Table I.

TABLE I. Wind turbine control properties from Jonkman *et al.* (2009).

	cut-in	rated	cut-out
wind speed at the hub	3 m s ⁻¹	11.4 m s ⁻¹	25 m s ⁻¹
rotor speed	6.9 rpm	12.1 rpm	0 rpm

3. Propagation model

Sound propagation in the atmosphere is determined by solving a parabolic equation (PE) proposed in Ostashev *et al.* (2020) that accounts for a moving atmosphere without relying on an effective sound speed approximation. The results in Colas *et al.* (2023) have shown that this PE yields excellent agreement with numerical solutions of the linearized Euler equations

Noise levels and amplitude modulation for two interacting wind turbines for a wind turbine in flat terrain. Note that a modified PE that better handles the sound speed gradients has also been proposed and analyzed in [Ostashev *et al.* \(2024\)](#).

The propagation simulation is carried out using the N×2D-PE propagation method: two-dimensional simulations are performed in vertical planes for several azimuthal angles τ around each source. This approach provides three-dimensional acoustic fields but neglects horizontal refraction. The PE is solved using the Crank-Nicolson method with a uniform grid step set to a tenth of the wavelength. A perfectly matched layer is used as a non-reflecting boundary condition at the top of the domain. At the ground, an impedance boundary condition is implemented. The surface impedance is prescribed using the variable porosity model ([Attenborough *et al.*, 2011](#)) with a flow resistivity of 50 kN s m^{-4} and a porosity change rate of 100 m^{-1} , representing a grassy ground. In addition, the projection of the horizontal mean flow velocity in the propagation plane is determined from the LES data. The sound speed is constant and is set to $c_0 = 340 \text{ m s}^{-1}$.

The rotor is discretized with an angular step $\Delta\beta = 10^\circ$ and each blade is divided into 8 segments. This yields a total of 288 source positions for each turbine. To reduce the number of simulations and the computational cost, the approach proposed in [Cotté \(2019\)](#) and used in [Colas *et al.* \(2023\)](#) is employed: propagation simulations are only performed for seven fictive sources distributed at different heights along the rotor centreline. The sound pressure level relative to the free-field level for each actual source position, denoted $\Delta L(m, \beta, f)$, is then determined from those of the fictive sources using interpolation.

The computational domain around each wind turbine extends 1 km upstream, 4 km downwind and 3.44 km crosswind. An angular step of 2° is used to discretize the whole

Noise levels and amplitude modulation for two interacting wind turbines domain except in the downwind direction ($-16^\circ < \tau < 16^\circ$) where a 1° angular step is used. This is done to better account for the wake effect in this direction. The results are then interpolated onto a uniform Cartesian grid with a grid step of 10 m to facilitate post-processing in configurations involving multiple wind turbines. The simulations are performed for a set of frequencies between 50 Hz and 1080 Hz.

4. *Chaining methodology*

The chaining methodology detailed in [Colas *et al.* \(2023\)](#) is employed. The flow properties are used to feed the source and propagation models. The sound pressure levels (SPL) from the wind turbines are obtained by combining the free-field levels predicted by the source model with the relative levels determined by the propagation model.

In more details, the SPL due to a given segment is computed with:

$$\text{SPL}(m, \beta, f) = \text{SPL}_{\text{ff}}(m, \beta, f) + \Delta L(m, \beta, f) - \alpha(f)R \quad (1)$$

with α the atmospheric absorption coefficient computed from [ISO 9613-1 \(1993\)](#) and R the source-receiver distance. To compute the SPL generated by two turbines operating at different rotor speeds, it is more convenient to work with time-domain signals rather than angular-domain signals. To do so, we express the SPL as a function of the receiver time, as done in [Mascarenhas *et al.* \(2022\)](#). We first note that the time-domain signal is periodic with period $2\pi/(3\Omega)$. Considering a time step Δt , the SPL due to a blade located at $t = 0$ at $\beta = 0^\circ$ is written:

$$\text{SPL}(t_k, f) = 10 \log_{10} \left(\sum_m 10^{\text{SPL}(m, \beta_j, f)} \delta_{m, j, k} \right), \quad (2)$$

with $t_k = k\Delta t$. The function $\delta_{m,j,k}$ is given by:

$$\delta_{m,j,k} = \begin{cases} 1, & \text{if } T_{m,j} < t_k < T_{m,j+1} \\ 0, & \text{otherwise} \end{cases} \quad (3)$$

where $T_{m,j}$ is the arrival time at the receiver of the contribution from the segment m at rotor angle $\beta_j = j\Delta\beta$. For simplicity, we assume that the propagation occurs along a straight line with constant sound speed $c_{\text{ref}} = c_0$, leading to:

$$T_{m,j} = \frac{R_{m,j}}{c_{\text{ref}}} + \frac{\beta_j}{\Omega} \quad (4)$$

where $R_{m,j}$ is the distance from the blade segment to the receiver.

The SPL due to the wind turbine as a function of time is then obtained by logarithmically summing the time signals of the three blades. The same methodology is applied to compute the SPL due to two turbines. Finally, the OASPL is obtained by integrating the SPL over the frequency band of interest. Two quantities of interest are derived from the OASPL: the average OASPL, denoted $\overline{\text{OASPL}}$, and the amplitude modulation (AM), defined as the difference between the maximum and minimum values of the OASPL.

The time step Δt must be chosen smaller than the minimum value of $\Delta\beta/\Omega$, which is approximately 0.14 s. In the following, Δt is set to 0.1 s. We have checked that further reduction of Δt yields negligible changes in the average OASPL and AM.

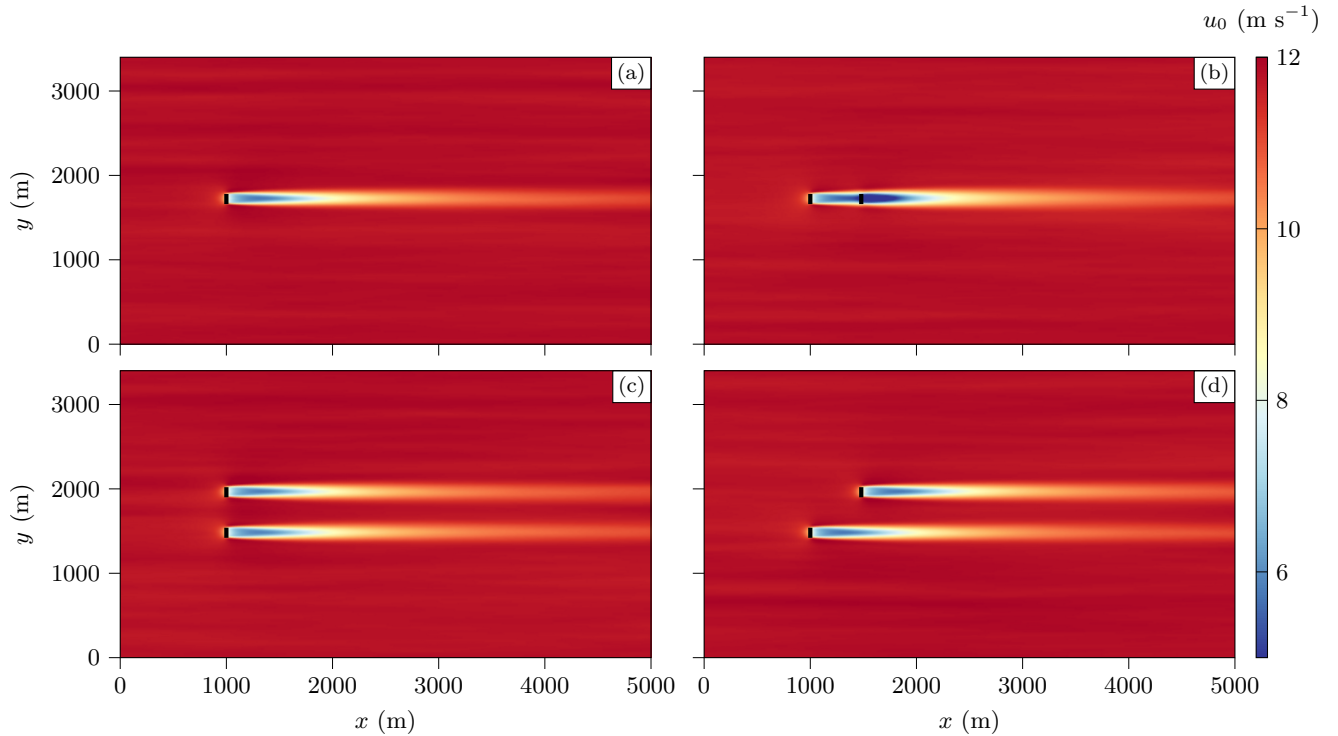


FIG. 2. Magnitude of the mean flow streamwise velocity at hub height for the four cases: (a) B, (b) C, (c) L, and (d) S. The rotors of the wind turbines are represented by a thick black line.

III. FLOW, SOURCE, AND PROPAGATION

A. Flow

The mean streamwise velocity u_0 is shown at hub height for the four configurations in Fig. 2. For case B in Fig. 2 (a), we observe the wake behind the turbine, which extends downstream up to several kilometers. For case C in Fig. 2 (b), we note the two wakes superimposing on each other, creating a stronger velocity deficit behind the second turbine. For cases L (Fig. 2 (c)) and S (Fig. 2 (d)), the wakes behind each turbine can be distinguished, without any noticeable wake interaction.

B. Source

The source model uses as input the profiles of the mean flow velocity and of the turbulent dissipation rate in the rotor plane of the turbines. These profiles are all nearly identical, except for turbine C2 which is positioned in the wake of turbine C1. The source model provides as output the SPL in the free field for each blade segment at every angular position. From this, we can determine the sound power level in the free field, denoted SWL, and the overall sound power level integrated over the frequency band of interest, denoted OASWL. As for the sound pressure level, averaged values of the power levels and associated AM can then be computed.

Note that the sound powers presented below do not correspond to the actual ones, determined from the integration of the acoustic field over a surface enclosing the source. Instead, they are effective powers obtained from a single receiver located downwind. In more detail, the power levels are computed from the relation $\text{SWL} = \text{SPL}_{\text{ff}} + 10 \log_{10}(4\pi R^2)$, where the sound pressure level in the free field SPL_{ff} is evaluated at a downwind receiver sufficiently far from the turbine and R is the source-receiver distance. This effective power is introduced to compare sound production by the turbines in the downwind direction.

Figure 3 shows the profiles of the mean streamwise velocity and the turbulent dissipation rate ϵ_0 along the rotor centreline for both turbines in case C. The corresponding profiles of the ABL flow are also plotted as reference. We note for C1 a reduction of the wind speed at the rotor due to a blockage effect and the increase of the turbulence dissipation rate at the outer part of the rotor. For C2, as it is positioned in the wake of C1, the profiles

are significantly different. Along the rotor, the velocity decreases compared to that of C1. Simultaneously, the turbulent dissipation rate strongly increases, especially at the top of the rotor.

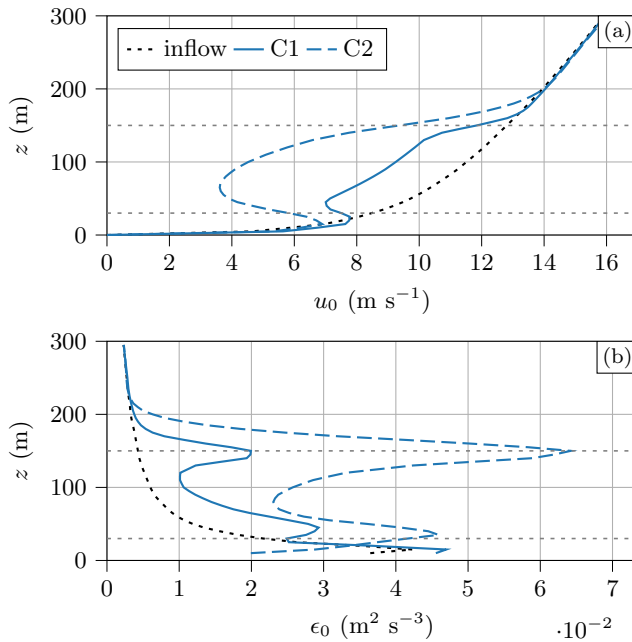


FIG. 3. Profile of (a) the streamwise velocity u_0 and (b) the turbulent dissipation rate ϵ_0 along the rotor centreline for the two wind turbines in case C. The rotor edges are visualized with gray dotted horizontal lines. The inflow profiles are also represented for reference.

The effects of the different flow profiles on the source model are illustrated in Fig. 4. Fig. 4 (a) shows the spectrum of the average source power level in the free field $\overline{\text{SWL}}$ for the wind turbines C1 and C2. The spectrum for C1 is composed of two humps of equal amplitude, the low-frequency one corresponding to TIN and the high-frequency one to TEN. The spectrum for C2 shows a global reduction in its amplitude because of the smaller wind velocity in the rotor plane. The hump at low frequencies has a higher amplitude than that

Noise levels and amplitude modulation for two interacting wind turbines at high frequencies, because of the relative increase in TIN due to the increase in turbulent dissipation rate. The spectrum of amplitude modulation due to the source AM_{SWL} is plotted in Fig. 4 (b). It is small for both wind turbines, with values below 0.3 dBA. Note that the large spatial variations in the profiles for C2 do not lead to a significant increase in AM associated to the source. As a reminder, these source properties are calculated from a receiver located downwind. In particular, amplitude modulation is expected to be stronger in the crosswind direction.

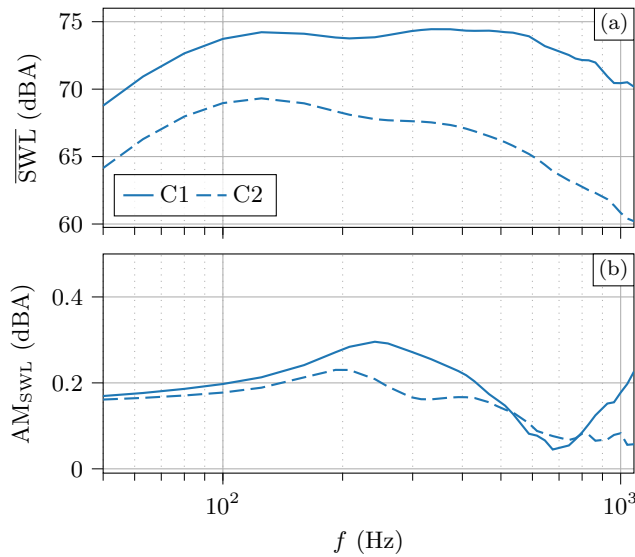


FIG. 4. Spectrum of (a) the average sound power level \overline{SWL} and (b) the corresponding amplitude modulation AM_{SWL} for the two turbines in case C.

For the four configurations, Table II gives the mean flow velocity and the turbulent dissipation rate at the hub, denoted u_{hub} and ϵ_{hub} , as well as the rotational speed of the rotor and the average OASWL of the turbines. These values are almost the same for all turbines except for C2. Indeed, the mean flow velocity at the hub for C2 is significantly

TABLE II. Source parameters computed for each wind turbine.

	B	C1	C2	L1	L2	S1	S2
u_{hub} (m s ⁻¹)	9.00	8.92	4.10	8.98	9.02	8.92	9.00
ϵ_{hub} (m ² s ⁻³)	0.012	0.012	0.024	0.012	0.012	0.012	0.012
Ω (rpm)	10.24	10.15	7.15	10.22	10.26	10.14	10.24
$\overline{\text{OASWL}}$ (dBA)	103.3	103.1	96.0	103.2	103.4	103.0	103.4

smaller, resulting in a lower rotational speed. In addition, the sound power level of C2 is reduced by more than 7 dBA. Also, the wind speed at the hub differs by less than 0.5 % for L1 and L2, leading to nearly identical rotor speeds. For S1 and S2, the deviations in wind speed at hub height are slightly larger, around 0.9 %. Although small, these differences in rotor speed significantly affect the temporal signals, as discussed in Secs. [IV B](#) and [IV C](#).

The mean flow at the hub can differ between the two turbines because of mutual aerodynamic interaction. Note also that the mean velocity is obtained by time-averaging the instantaneous fields. Statistical convergence may have not been fully reached due to large-scale structures in the ABL. This may also induce difference between the mean flow at the hub for two turbines.

C. Propagation

This section presents the effect of the mean flow on sound propagation. For clarity, the analysis is limited to a single source positioned at the turbine hubs.

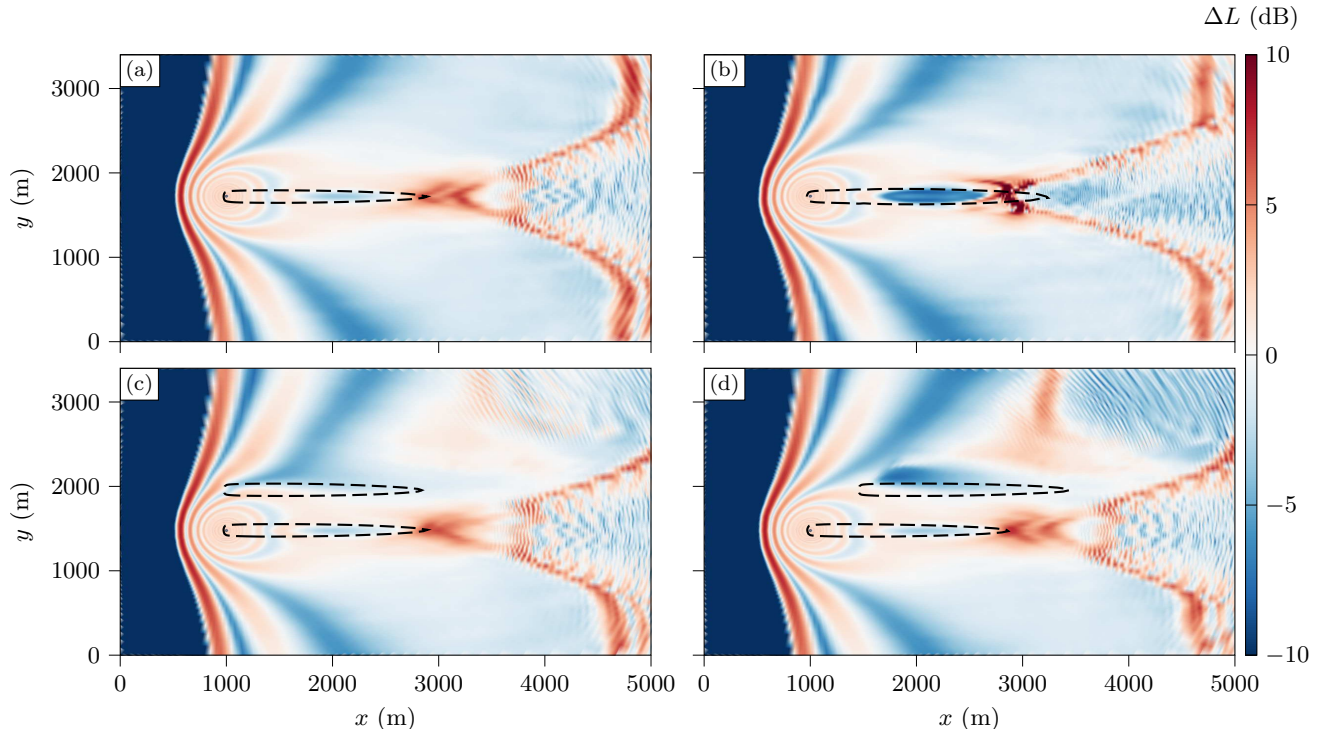


FIG. 5. Sound pressure level relative to the free-field level ΔL averaged over the third-octave band centered at 1 kHz at $z = 2$ m for a source at the hub height for the wind turbines: (a) B, (b) C1, (c) L1, and (d) S1. The black dashed lines correspond to $u_0(z = 90\text{m}) = 10 \text{ m s}^{-1}$ and aim at highlighting the wake regions.

Fig. 5 shows the ΔL at 2 m height averaged over the third-octave band centered at 1 kHz for a point source at the hub of turbines B, C1, L1, and S1. The contour lines of the mean flow streamwise velocity for 10 m s^{-1} are overlaid as black dashed lines to indicate the wake regions. Fig. 6 displays the same data in a 3D view to highlight the influence of multiple wakes on noise amplification at the ground. For case B in Fig 5 (a) and Fig 6 (a) we note several characteristics of sound propagation in the flow of an isolated wind turbine (Barlas *et al.*, 2017b; Colas *et al.*, 2024; Heimann *et al.*, 2018). Upwind, a shadow zone is generated

for $x < 800$ m with high levels at its boundary. Downwind, an amplification of the sound levels at the ground is seen in the flow direction ($\tau = 0^\circ$) at $x = 3000$ m due to wake focusing. As the propagation angle increases, focusing at the ground moves away, resulting in a V-shaped amplification zone. Finally, for sufficiently large propagation angles, sound waves do not cross the wake. Focusing observed at $x = 4700$ m, independent of the y -direction, is instead caused by the velocity gradient in the ABL.

The wake superposition in case C has a significant effect on sound propagation downwind, see Fig. 5 (b). Focusing in the flow direction is stronger and closer to the turbine by 100 m compared to the baseline case. This is induced by the second wake as shown in Fig 6 (b). Two focusing zones appear just after the second turbine due to the large velocity gradients at the top and bottom of the rotor that efficiently redirect sound waves toward the ground. This is similar to what was shown in Sun *et al.* (2018). The V-shaped pattern in the ΔL field after this initial focusing is still visible and does not seem to be strongly affected by the second wake.

The second wake also has an effect for layouts L and S, but it is less pronounced. Figs. 5 (c) and 5 (d) show an increase in ΔL downstream for propagation directions that intersect the wake of the second turbine. This effect is more pronounced in case S than in case L. In fact, the impact of the wake depends not only on the velocity deficit but also on the propagation angle. Specifically, for a propagation angle τ , considering only the streamwise component of the mean flow velocity, the wind speed projected onto the propagation direction is $u_0 \cos \tau$. For a given velocity deficit, the influence of the second wake becomes more significant as τ approaches zero. Consequently, in case S, as propagation angles intersecting the second wake

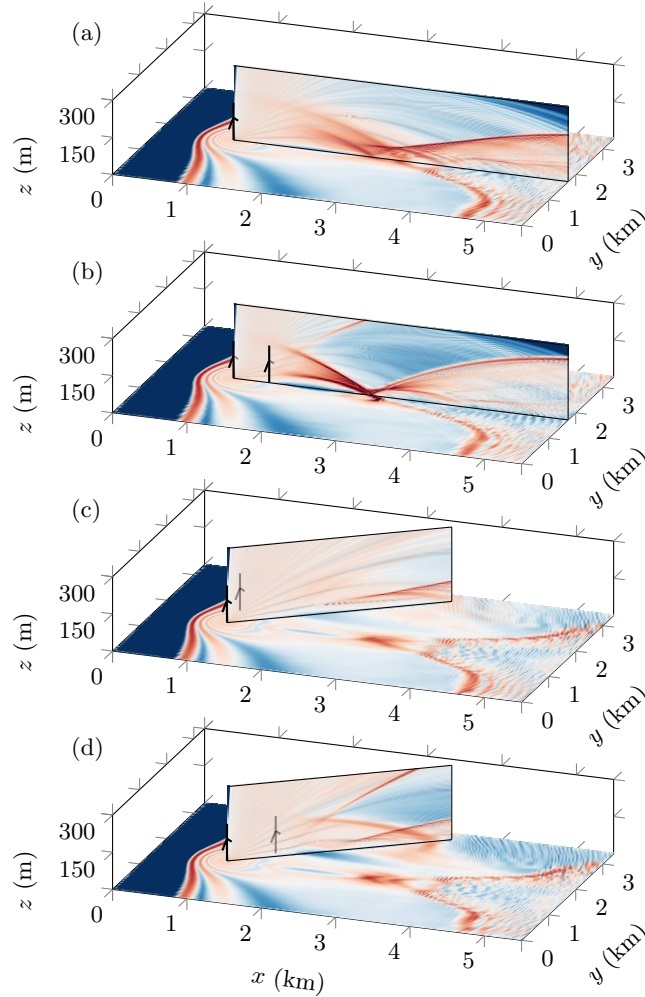


FIG. 6. Sound pressure level relative to the free-field level ΔL averaged over the third-octave band centered at 1 kHz for a horizontal plane at 2 m height and a vertical plane at (a, b) $\tau = 0^\circ$ and (c, d) $\tau = 35^\circ$. The source is located at the hub of the wind turbines: (a) B, (b) C1, (c) L1, and (d) S1. The color range is the same as in Fig. 5.

are smaller, refraction is stronger. Conversely, in case L, the propagation angles intersecting the second wake are larger, leading to small variations in the projected wind speed and, therefore, to reduced refraction effects by the second wake. This is illustrated in Figs. 6 (c) and 6 (d) where focusing induced by the second wake is more noticeable in case S than in

Noise levels and amplitude modulation for two interacting wind turbines case L for the same propagation angle ($\tau = 35^\circ$). In addition, focusing caused by the ABL velocity gradient at $x = 4700$ m visible for cases B and C in Figs. 5 (a) and (b) is no longer observed for $y > 2500$ m for cases L and S in Figs. 5 (c) and (d). Finally, a region of lower ΔL is also present just after the second wake in Fig. 6 (d).

To help understand the refraction of sound waves by the flow, ray-tracing simulations are carried out following [Candel \(1977\)](#) and [Scott *et al.* \(2017\)](#). The rays are presented in Fig. 7 for side planes corresponding to those shown in Fig. 6. They are superimposed onto the projection of the horizontal component of the flow velocity onto the considered plane. In Fig. 7, r denotes the horizontal distance from the source. For the baseline case B in Fig 7 (a), we observe focusing induced by the wake. This leads to a high density of rays close to the ground for $1900 \text{ m} < r < 2000 \text{ m}$, which corresponds to the increase in ΔL at the ground in Fig. 5 (a). Moreover, a caustic starting at $r = 2000$ m and $z = 50$ m is also observed and its position coincides with the rise in ΔL visible in Fig. 6 (a).

For turbine C1 (Fig. 7 (b)), the wake of turbine C2 acts as a converging lens that enhances focusing. This leads to the formation of a caustic in the wake of C2, with a focal point at $r = 1340$ m and $z = 78$ m, which impacts the ground around $r = 1900$ m. This explains the large increase in ΔL observed at this position in Fig. 6 (b).

The difference between the refraction induced by the second wake for cases L and S is illustrated in Figs. 7 (c) and (d) for $\tau = 35^\circ$. Since the velocity deficit due to the wake in the propagation plane is more pronounced in case S than in L, the refraction induced by the second wake is stronger in the former case.

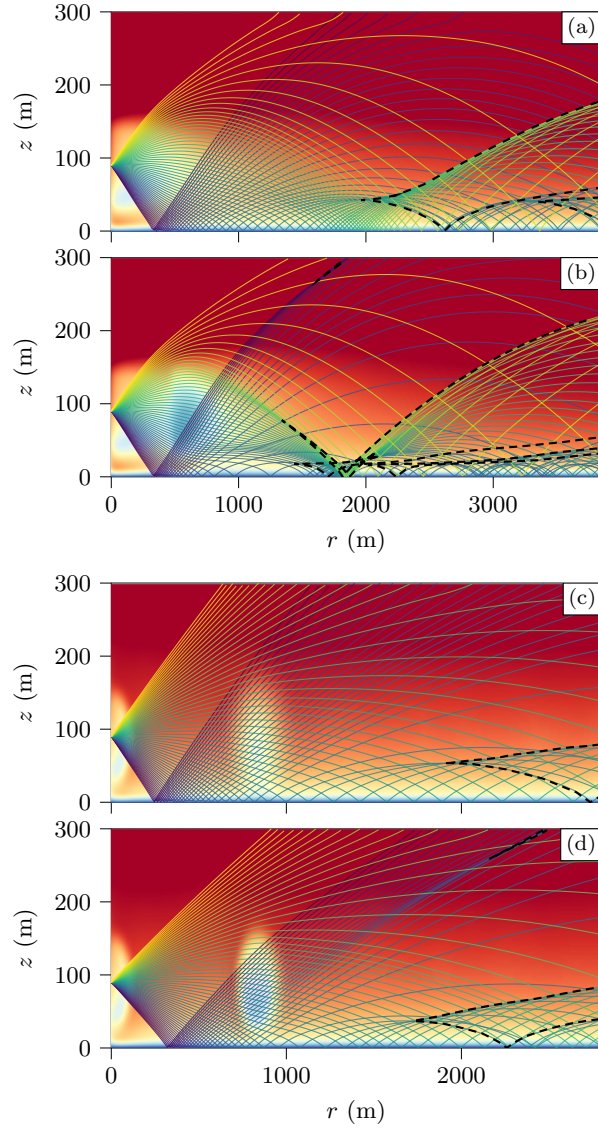


FIG. 7. Ray tracing for turbine (a) B and (b) C1 for a propagation angle $\tau = 0^\circ$ and for turbine (c) L1 and (d) S1 for $\tau = 35^\circ$. Rays are superimposed on the projected horizontal flow velocity field in the propagation plane, while caustics are depicted as black dashed lines. The color range for the velocity magnitude is the same as in Fig. 2.

The converging lens effect induced by the second wake is clearly visible in case S in Fig. 7 (d). Bundles of rays passing through the second wake are refracted inward, resulting

Noise levels and amplitude modulation for two interacting wind turbines in amplified sound pressure levels. Thus, the rays launched downwards and then reflected from the ground before crossing the second wake generate a caustic at $r = 2150$ m and $z = 260$ m in Fig. 7 (d). Similarly, the region of increased levels visible in Fig. 6 (d) that intersects the ground at a large distance can be associated with a bundle of rays launched upwards, then refracted downwards by the ABL velocity gradient, and finally focused due to the crossing of the second wake. We also observe that the presence of the second wake tends to shift the caustic associated with the ABL velocity gradient closer to the source: thus, this caustic is located at the ground level 4.3 km from the source without a second wake, but 2.9 km in case L and 2.3 km in case S. Finally, the coarser ray density after the second wake for case S in Fig. 7 (d) is in agreement with the reduced value of ΔL in Fig. 6 (d).

IV. NOISE FROM THE WIND TURBINE PAIR

A. Statistical results

Using the methodology from Sec. II, the instantaneous OASPL fields are computed from the results in Sec. III, accounting for the rotation of the wind turbine blades. From these, the average OASPL and the AM fields are determined.

1. Average sound pressure levels

The $\overline{\text{OASPL}}$ fields at 2 m height are shown in Fig. 8 for the four cases. For the baseline case B in Fig. 8 (a), we find several characteristics of the noise generated by an isolated wind turbine, including a dipolar directivity with cross-wind extinction zone, a shadow zone

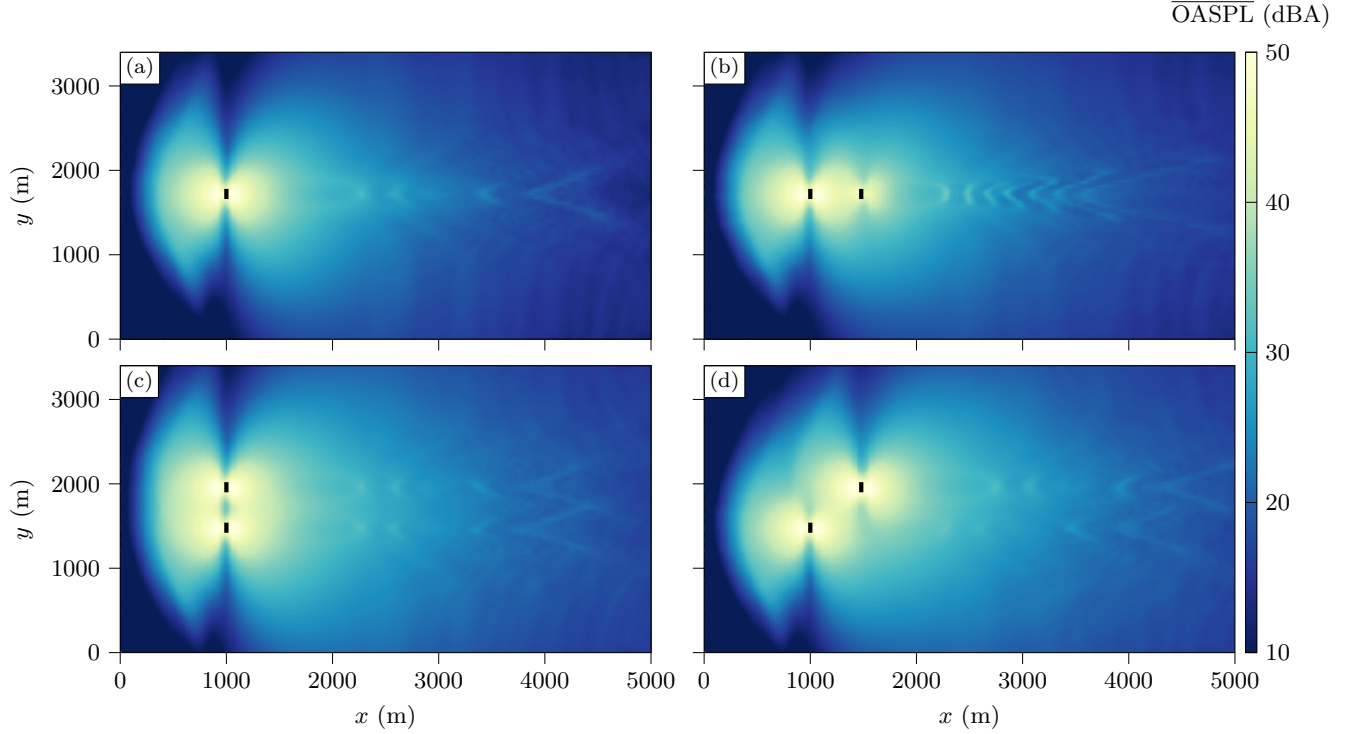


FIG. 8. Average overall sound pressure levels $\overline{\text{OASPL}}$ at $z = 2$ m for the four cases: (a) B, (b) C, (c) L, and (d) S.

upwind, for $x < 400$ m, and focusing patterns downwind due to the wake. Fig. 8 (b) shows the $\overline{\text{OASPL}}$ field for case C with the contributions of the two wind turbines accounted for. The downstream turbine (C2) contribution is smaller due to the modified inflow conditions induced by the upstream turbine wake causing a reduction in sound power level (as described in Sec. III B). The upwind shadow zone and crosswind extinction zones of the first turbine closely resemble those of case B. The crosswind extinction zones of the second turbine are barely visible due to the contribution of the first turbine that brings significant energy in these zones. The downwind focusing pattern also shows some differences, with more pronounced focusing in this case. The amplification at the ground is primarily due to the

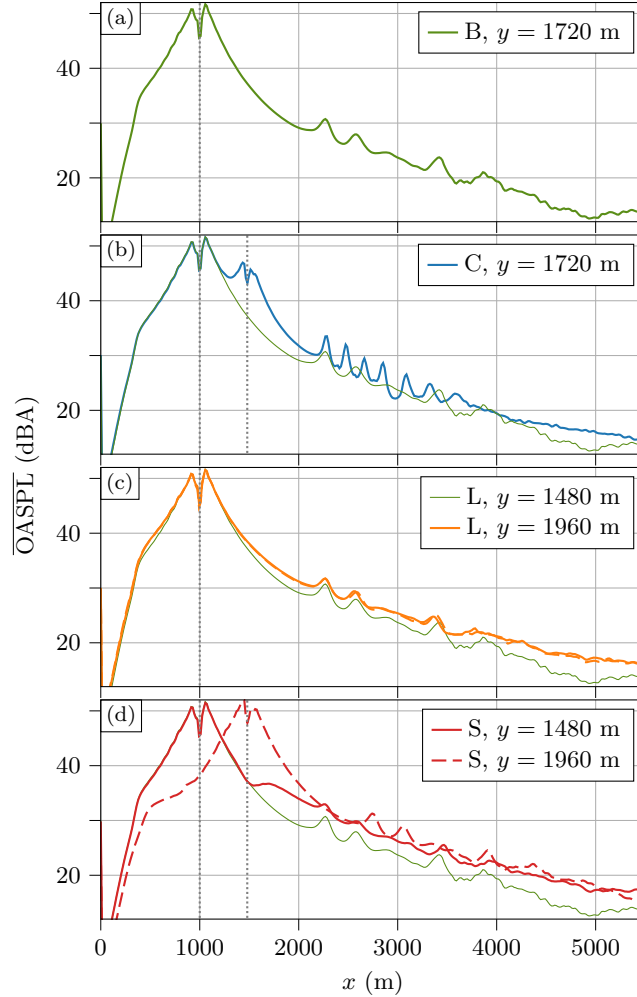


FIG. 9. Average overall sound pressure levels $\overline{\text{OASPL}}$ at $z = 2$ m along lines of receivers whose y -coordinate corresponds to the turbine positions in the four cases: (a) B, (b) C, (c) L, and (d) S. The gray dotted vertical lines correspond to the wind turbine positions. For comparison purposes, the result for B in (a) is reproduced in (b-d).

first wind turbine emission, which is strongly refracted by the second turbine wake (as shown in Sec. III C). In Figs. 8 (c) and (d), cases L and S display downwind focusing patterns that appear very similar to those obtained from a single wind turbine, in accordance with the limited interaction between the wakes observed for the mean velocity fields in Fig. 2.

The $\overline{\text{OASPL}}$ for the different cases is plotted in Fig. 9 along lines of receivers whose y -coordinate corresponds to the turbine positions at a height of 2 m. For case B in Fig. 9 (a), we note the overall decrease of the $\overline{\text{OASPL}}$ with distance, with a sharp decrease upwind for $x < 400$ m due to the shadow zone. Wake focusing causes bumps in $\overline{\text{OASPL}}$ downwind at $x = 2250$ m and 3400 m, with a maximum increase of 3 dBA.

Cases C, L, and S in Figs. 9 (b), (c), and (d), respectively, show an overall increase downwind compared to the baseline case B due to the presence of two wind turbines instead of one. In particular, for case C in Fig. 9 (b), the $\overline{\text{OASPL}}$ rises significantly around $x = 1480$ m due the second wind turbine. Again for case C, focusing attributed to the superposition of the two wakes is visible for $2000 \text{ m} < x < 3500 \text{ m}$ with several narrow peaks. Additional simulations, not shown here for brevity, indicate that increasing the number of fictive sources in the source model introduces more peaks in the $\overline{\text{OASPL}}$ and fills the gaps between those in Fig. 9 (b). As a consequence, a continuous increase in $\overline{\text{OASPL}}$ between 4 and 5 dBA is expected in this region.

For case L in Fig. 9 (c), the curves for $y = 1480$ m and $y = 1960$ m, which both correspond to the location of the turbines, match almost perfectly. The $\overline{\text{OASPL}}$ increase induced by the wake effect is similar to that of the baseline case. Overall, levels are higher (about 1 dBA) downwind due to the contributions of both turbines. Finally, for case S in Fig. 9 (d), the peaks due to the wake also coincide with those of case B but are shifted by 480 m for the line at $y = 1960$ m (aligned with turbine S2) because of the turbine position offset. For the line at $y = 1480$ m (aligned with S1), the $\overline{\text{OASPL}}$ shows for $x > 1480$ m an overall increase by 3 dBA compared to case B, due to the contribution of S2. In particular, the presence of

S2 mitigates the increase in $\overline{\text{OASPL}}$ due to wake focusing, causing a reduction in the peak amplitude. Upwind, the shadow zone is consistent across all cases.

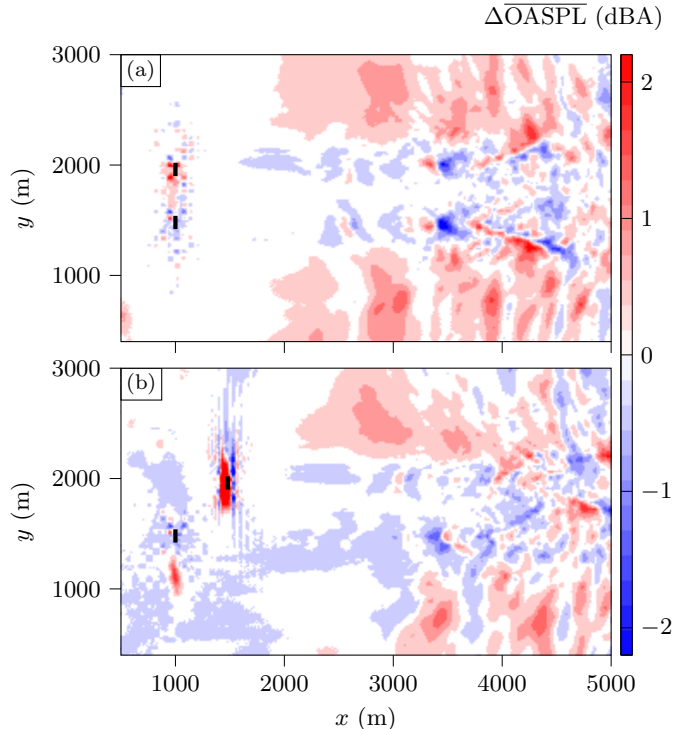


FIG. 10. Difference between the actual $\overline{\text{OASPL}}$ and that obtained using ΔL of turbine B in the plane $z = 2$ m for cases (a) L and (b) S.

To investigate the importance of the second wake on noise prediction, additional simulations are performed for cases S and L using ΔL computed for turbine B instead of the actual ΔL and keeping the same source properties. Fig. 10 shows the difference in $\overline{\text{OASPL}}$ between those obtained for the actual cases and those for the artificial cases in a plane at 2 m height. For case L (Fig. 10 (a)), there is an increase of 1-2 dBA induced by the second wake focusing off the x -axis for $x > 2000$ m and for $y < 1200$ m and $y > 2200$ m. In the downwind direction, SPL decreases by less than 1 dBA for $2000 \text{ m} < x < 3200 \text{ m}$. At $x = 3200$ m, the levels

abruptly increase before decreasing. This is due to a shift in focusing position between the reference case and the artificial one. This shift may come from the aerodynamic interactions between the two turbines or from small differences in the simulated flows between cases B and L.

In case S (Fig. 10 (b)) the difference induced by the second wake in the oblique direction ($x > 2000$ m and $y > 2200$ m, and $x > 3000$ m and $y < 1200$ m) is of the same order of magnitude, despite the stronger increase in ΔL described in Sec III C. In the downwind direction, a reduction by less than 1 dBA is observed for $x < 4500$ m. Abrupt variations in $\overline{\text{OASPL}}$ are also noticed due to a shift in the focusing patterns at the ground as for case L.

2. *Amplitude modulation*

The AM fields at 2 m height are plotted for the four cases in Fig. 11. For case L, since the wind turbines operate at nearly identical rotational speeds, AM depends on the angular offset between the two rotors. In this section, we assume no angular offset; its impact on AM is discussed in Sec. IV B. Case B in Fig. 11 (a) shows cross-wind AM induced by the blade rotation, upwind AM at the shadow zone boundary, and downwind AM due to wake focusing for $x > 2000$ m. Similar AM patterns are observed for the other three cases. For case C in Fig. 11 (b), the AM downwind is significantly enhanced, which is expected due to the stronger focusing effect caused by the second wake. The downwind turbine C2 does not generate crosswind AM, as its acoustic power is considerably smaller than that of the upwind turbine C1. For cases L and S in Figs. 11 (c) and (d), both crosswind and downwind AM are lower than that in the baseline case. This is due to the combined contributions

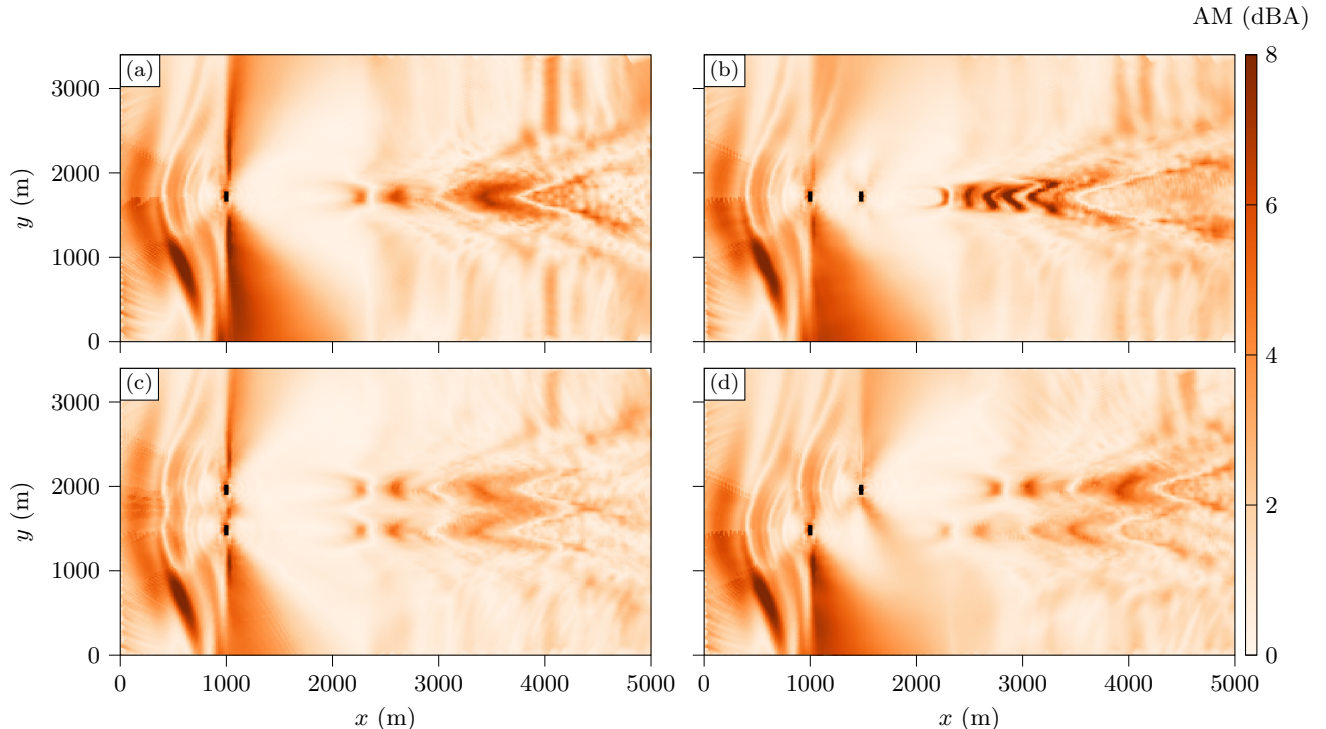


FIG. 11. Amplitude modulation at $z = 2$ m for the four cases: (a) B, (b) C, (c) L, and (d) S.

of the two turbines, which tend to reduce the difference between minimum and maximum OASPL observed at a given receiver. For case S in Fig. 11 (d), downwind AM is stronger at $y = 1960$ m than at $y = 1480$ m. Indeed, at $y = 1960$ m, the contribution of turbine S1 is small compared to that of S2 and hence the AM due to S2 is close to the one obtained for the baseline case downwind. On the contrary at $y = 1480$ m, the contribution of S2 is significant so that AM due to S1 is reduced compared to case B.

As in Sec. IV A 1, AM is plotted along lines of receivers whose y -coordinate corresponds to the turbine positions at a height of 2 m for the different cases in Fig. 12. For case B (Fig. 12 (a)), significant values of AM are obtained upwind (around 4 dBA) and downwind (around 7 dBA). For case C in Fig. 12 (b), the downwind increase is more pronounced with

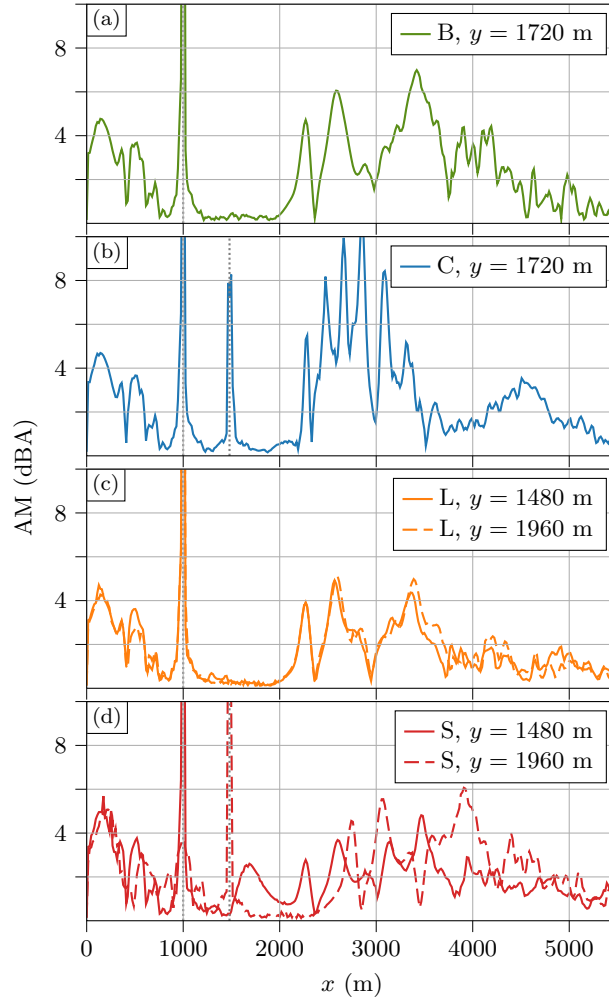


FIG. 12. Amplitude modulation at $z = 2$ m along lines of receivers whose y -coordinate corresponds to the turbine positions for the four cases: (a) B, (b) C, (c) L, and (d) S.

AM reaching up to 10 dBA. It also appears more localized within the range $2100 \text{ m} < x < 3500 \text{ m}$, corresponding to the zone of increased $\overline{\text{OASPL}}$ due to wake effects (see Fig. 9 (b)). Cases L and S in Figs. 12 (c) and (d) exhibit similar AM patterns to case B but the maximum values are lower downwind (around 5 dBA).

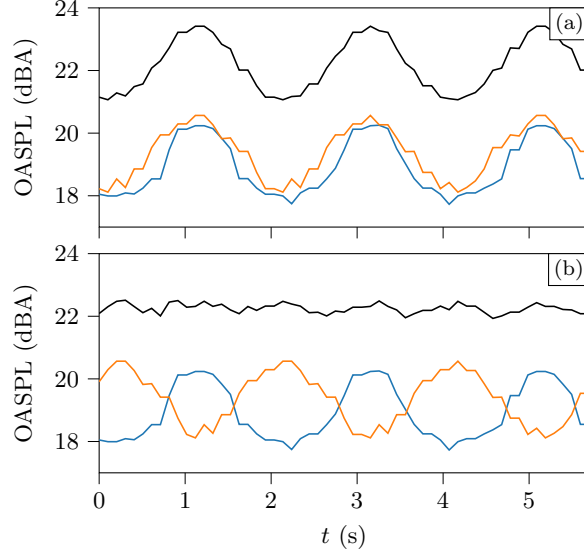


FIG. 13. Temporal signals of OASPL for case L at $\mathbf{x} = (3000, 1720, 2)$ m for (a) $\Delta\beta_{1-2} = 0^\circ$ and (b) $\Delta\beta_{1-2} = 60^\circ$. The total signal is plotted in black and the contributions of each turbine are plotted in blue and orange.

B. Synchronization effect

For case L, the two turbines operate under almost identical mean flow conditions and rotate at nearly the same speed, as indicated in Tab. II. As a consequence, the sound field depends on the relative angular position of the two turbine rotors. We denote by $\Delta\beta_{1-2}$ the offset between the angular position of the turbine rotors (see Fig. 1). Fig. 13 illustrates this effect at a receiver located downwind in between the two turbines at a distance of 2 km. In Fig. 13 (a), the angular position of the rotor is the same for the two turbines ($\Delta\beta_{1-2} = 0^\circ$). The time-varying SPL due to each wind turbine are in phase, resulting in AM of around 2 dBA. In Fig. 13 (b), the blades of the two turbines rotate with an angular offset of $\Delta\beta_{1-2} = 60^\circ$. In this case, the SPL signals are out of phase leading to AM close

to zero. Note that this effect is not due to constructive or destructive interference. The SPL signals due to the two turbines are summed incoherently, meaning the average OASPL remains the same in both cases, despite the difference in AM.

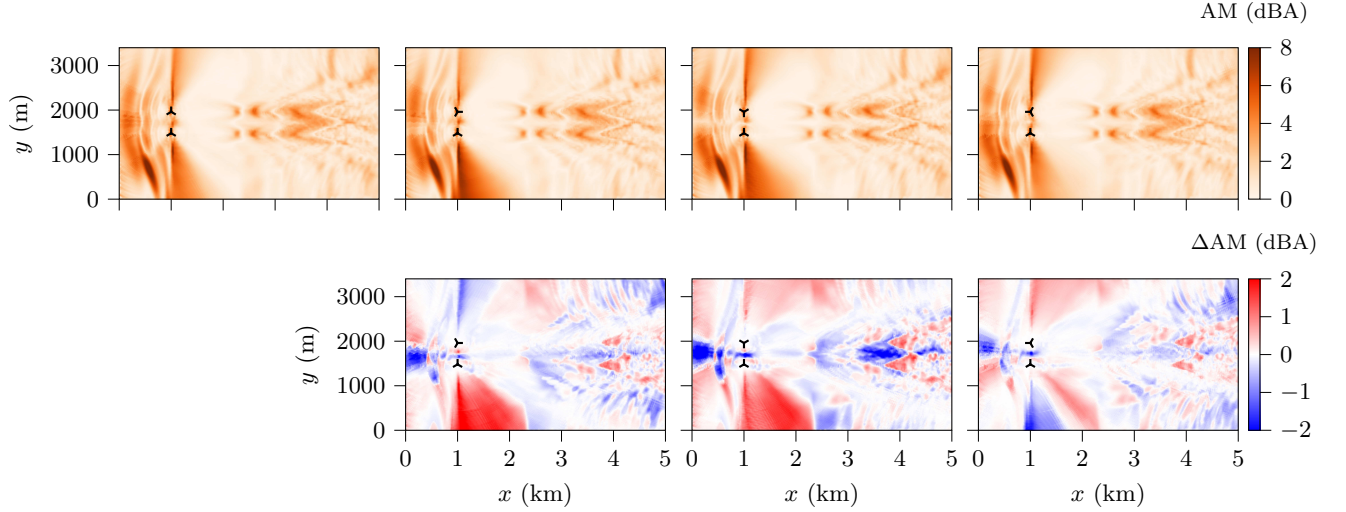


FIG. 14. (top) AM in case L for several angular offsets ($\Delta\beta_{1-2}$) between the turbine rotors. From left to right, $\Delta\beta_{1-2} = 0, 30, 60,$ and 90° . (bottom) Difference between AM obtained with several offsets and AM without offset ($\Delta\beta_{1-2} = 0^\circ$). Turbine positions are represented by the three blades of the rotor to help visualize the angular offset.

We further illustrate this effect in Fig. 14. The AM fields at 2 m height are presented for several offsets between the turbine rotors. The difference between the AM obtained for a given value of $\Delta\beta_{1-2}$ and that for $\Delta\beta_{1-2} = 0^\circ$ is also depicted. The AM patterns remain qualitatively similar for the different angular offsets, consistently exhibiting increased AM in the crosswind, upwind, and downwind directions. However, AM magnitude depends on $\Delta\beta_{1-2}$. In the zone exactly between both turbines downwind (around $x = 3500$ m) and upwind (around $x = 500$ m), AM decreases as $\Delta\beta_{1-2}$ increases and reaches almost 0 dBA

Noise levels and amplitude modulation for two interacting wind turbines for $\Delta\beta_{1-2} = 60^\circ$, which corresponds to the turbines being in phase opposition. On the contrary, the crosswind AM increases by up to 2 dBA when the turbines are out of phase.

Whether the signals from the two turbines are in or out of phase depends on several factors, including the angular offset between the turbine rotors and the propagation time. Finally, we remind the reader that if the rotational speeds of the turbines are different, the statistical properties of the sound field do not depend on the relative angular position of the turbine rotors.

C. Beating effect

In cases C and S, the turbine rotors do not rotate at the same speed. Consequently, the temporal signal of OASPL due to each turbine has a different period. When the rotational speeds are close, as in case S, a beating effect can be observed at positions where the contributions of both turbines are of the same order of magnitude. In these locations, the signal is modulated by an envelope with a frequency lower than the blade-passing frequency. For case C, the rotational speeds of the two turbines are too different to observe this beating effect.

As an example, the OASPL signals for case S at two receiver locations are plotted in Fig. 15. Fig. 15 (a) is obtained for a receiver located crosswind and Fig. 15 (b) for a downwind receiver located between the two turbines. The signals at both positions alternate between discernible AM (2 dBA crosswind and 3 dBA downwind) and much smaller AM (close to zero crosswind and 1 dBA downwind).

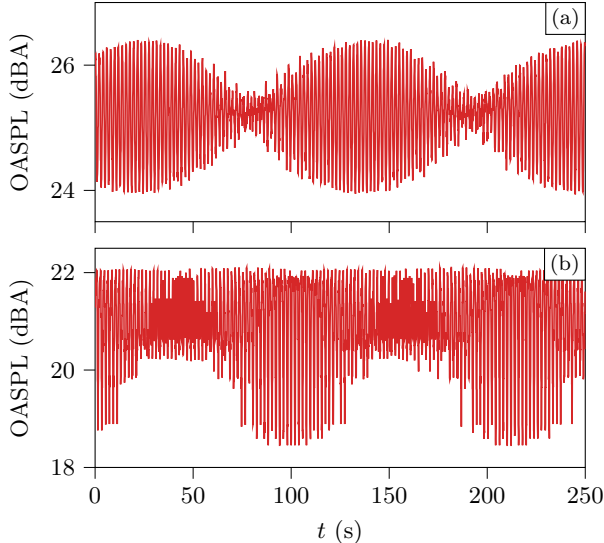


FIG. 15. Temporal signals of OASPL for case S at (a) $\mathbf{x} = (1500, 2500, 2)$ m and (b) $\mathbf{x} = (4400, 1720, 2)$ m.

The carrier frequency f_c and envelope frequency f_e of the OASPL signal can be derived from trigonometric relations, yielding:

$$f_c = \frac{f_1 + f_2}{2}, \quad f_e = \frac{f_1 - f_2}{2}, \quad (5)$$

where f_1 and f_2 are the blade passing frequencies of each turbine ($f = 3\Omega/(2\pi)$). Consequently, the carrier and envelope frequencies are identical at different receiver positions. Considering the rotational speeds of the turbines S1 and S2 in Tab. II, we obtain $f_e = 0.0045$ Hz which corresponds to a period of 222 s. This value matches the period of the envelope observed for the signals in Fig. 15. Moreover, Fig. 15 shows that the largest values of AM occur at different times between crosswind and downwind receivers due to varying propagation times between the sources and the receiver.

The beating effect was reported in field experiments for stable atmospheric conditions in [van den Berg \(2005\)](#). This phenomenon introduces a second layer of variability with intermittency in AM. From a perceptual point of view, this suggests that AM can be likely imperceptible to occasionally perceptible ([Nguyen *et al.*, 2021](#)).

V. CONCLUSION

A numerical study of noise propagation from a pair of wind turbines was presented, focusing on how the wake of a second turbine modifies the acoustic field of the first. The most significant effects occur when the turbines are aligned with the flow direction. For the upstream turbine, the second wake enhances wake focusing leading to increased average OASPL and AM downwind compared to an isolated wind turbine. The downstream turbine exhibits a significant reduction in noise emission due to decreased inflow velocity at the rotor plane, resulting from its position within the wake of the upstream turbine.

When the two turbines are side-by-side or staggered, propagation effects remain moderate. An increase in the average OASPL by less than 2 dBA has been noticed in the oblique direction downwind. Moreover, AM is reduced compared to that of an isolated wind turbine, since the superposition of signals from both turbines tends to smooth out the noise level fluctuations, which reduces the difference between maximum and minimum sound pressure levels.

An important aspect of the analysis involves the temporal evolution of the OASPL at a receiver. When turbines rotate at nearly identical speeds, the angular offset between the rotors significantly impacts the temporal signal, leading to variations in AM. However,

Noise levels and amplitude modulation for two interacting wind turbines when rotor speeds differ slightly, the signal exhibits prominent beating effects, creating clear intermittency in AM. This behavior is especially important because it highlights a strong sensitivity of AM characteristics to small differences in rotor dynamics. Understanding this sensitivity is crucial for accurately capturing noise variability and its perceptual effects.

Future work could include comparison with experiments and a relaxation of current modeling assumptions, particularly by accounting for three-dimensional propagation and scattering by turbulence. Effects of wind turbine interactions on noise propagation could also be investigated at wind farm level for further understanding. Finally, integration of these interaction effects into operational models could be studied.

ACKNOWLEDGMENTS

This work was performed within the framework of the LABEX CeLyA (ANR-10-LABX-0060) of Université de Lyon, within the program “Investissements d’Avenir” (ANR-16-IDEX-0005) operated by the French National Research Agency (ANR). This project has received funding from the European Research Council under the European Union’s Horizon Europe program (Grant No. 101124815). It was granted access to the HPC resources of PMCS2I (Pôle de Modélisation et de Calcul en Sciences de l’Ingénieur et de l’Information) of Ecole Centrale de Lyon. This work was supported by the Franco-Dutch Hubert Curien partnership (Van Gogh Programme No. 49310UM). For the purpose of Open Access, a CC-BY public copyright license has been applied by the authors to the present document and will be applied to all subsequent versions up to the Author Accepted Manuscript arising from this submission.

AUTHOR DECLARATIONS

The authors have no conflicts to disclose.

DATA AVAILABILITY

Data available on request from the authors.

Attenborough, K., Bashir, I., and Taherzadeh, S. (2011). “Outdoor ground impedance models,” *Journal of the Acoustical Society of America* **129**(5), 2806–2819, doi: [10.1121/1.3569740](https://doi.org/10.1121/1.3569740).

Barlas, E., Wu, K. L., Zhu, W. J., Porté-Agel, F., and Shen, W. Z. (2018). “Variability of wind turbine noise over a diurnal cycle,” *Renewable Energy* **126**, 791–800, doi: [10.1016/j.renene.2018.03.086](https://doi.org/10.1016/j.renene.2018.03.086).

Barlas, E., Zhu, W. J., Shen, W. Z., Dag, K. O., and Moriarty, P. (2017a). “Consistent modelling of wind turbine noise propagation from source to receiver,” *Journal of the Acoustical Society of America* **142**(5), 3297–3310, doi: [10.1121/1.5012747](https://doi.org/10.1121/1.5012747).

Barlas, E., Zhu, W. J., Shen, W. Z., Kelly, M., and Andersen, S. J. (2017b). “Effects of wind turbine wake on atmospheric sound propagation,” *Applied Acoustics* **122**, 51–61, doi: [10.1016/j.apacoust.2017.02.010](https://doi.org/10.1016/j.apacoust.2017.02.010).

Bommidala, H., Colas, J., Emmanuelli, A., Dragna, D., Khodr, C., Cotté, B., and Stevens, R. J. (2025). “Three-dimensional effects of the wake on wind turbine sound propagation

- using parabolic equation,” *Journal of Sound and Vibration* **608**, 119036, doi: <https://doi.org/10.1016/j.jsv.2025.119036>.
- Bresciani, A. P. C., Maillard, J., and Finez, A. (2024). “Wind farm noise prediction and auralization,” *Acta Acustica* **8**, 15, doi: [10.1051/aacus/2024007](https://doi.org/10.1051/aacus/2024007).
- Candel, S. M. (1977). “Numerical solution of conservation equations arising in linear wave theory: application to aeroacoustics,” *Journal of Fluid Mechanics* **83**(3), 465–493, doi: [10.1017/S0022112077001293](https://doi.org/10.1017/S0022112077001293).
- Colas, J., Emmanuelli, A., Dragna, D., Blanc-Benon, P., Cotté, B., and Stevens, R. J. A. M. (2023). “Wind turbine sound propagation: Comparison of a linearized Euler equations model with parabolic equation methods,” *Journal of the Acoustical Society of America* **154**(3), 1413–1426, doi: [10.1121/10.0020834](https://doi.org/10.1121/10.0020834).
- Colas, J., Emmanuelli, A., Dragna, D., Blanc-Benon, P., Cotté, B., and Stevens, R. J. A. M. (2024). “Impact of a two-dimensional steep hill on wind turbine noise propagation,” *Wind Energy Science* **9**(10), 1869–1884, doi: [10.5194/wes-9-1869-2024](https://doi.org/10.5194/wes-9-1869-2024).
- Cotté, B. (2019). “Extended source models for wind turbine noise propagation,” *Journal of the Acoustical Society of America* **145**(3), 1363–1371, doi: [10.1121/1.5093307](https://doi.org/10.1121/1.5093307).
- Drela, M. (1989). “XFOIL: An Analysis and Design System for Low Reynolds Number Airfoils,” in *Low Reynolds Number Aerodynamics*, edited by T. J. Mueller, Lecture Notes in Engineering, Springer, Berlin, Heidelberg, pp. 1–12, doi: [10.1007/978-3-642-84010-4_1](https://doi.org/10.1007/978-3-642-84010-4_1).
- Gadde, S. N., Stieren, A., and Stevens, R. J. A. M. (2021). “Large-Eddy Simulations of Stratified Atmospheric Boundary Layers: Comparison of Different Subgrid Models,” *Boundary-Layer Meteorology* **178**(3), 363–382, doi: [10.1007/s10546-020-00570-5](https://doi.org/10.1007/s10546-020-00570-5).

- Heimann, D., and Englberger, A. (2018). “3D-simulation of sound propagation through the wake of a wind turbine: Impact of the diurnal variability,” *Applied Acoustics* **141**, 393–402, doi: [10.1016/j.apacoust.2018.06.005](https://doi.org/10.1016/j.apacoust.2018.06.005).
- Heimann, D., Englberger, A., and Schady, A. (2018). “Sound propagation through the wake flow of a hilltop wind turbine-A numerical study,” *Wind Energy* **21**(8), 650–662, doi: [10.1002/we.2185](https://doi.org/10.1002/we.2185).
- ISO 9613-1 (1993). “Acoustics — Attenuation of sound during propagation outdoors — Part 1: Calculation of the absorption of sound by the atmosphere” .
- Jonkman, J., Butterfield, S., Musial, W., and Scott, G. (2009). “Definition of a 5-MW reference wind turbine for offshore system development,” Technical Report NREL/TP-500-38060, 947422, doi: [10.2172/947422](https://doi.org/10.2172/947422).
- Kayser, B., Cotté, B., Ecotière, D., and Gauvreau, B. (2020). “Environmental parameters sensitivity analysis for the modeling of wind turbine noise in downwind conditions,” *Journal of the Acoustical Society of America* **148**(6), 3623–3632, doi: [10.1121/10.0002872](https://doi.org/10.1121/10.0002872).
- Lee, S., Lee, D., and Honhoff, S. (2016). “Prediction of far-field wind turbine noise propagation with parabolic equation,” *Journal of the Acoustical Society of America* **140**(2), 767–778, doi: [10.1121/1.4958996](https://doi.org/10.1121/1.4958996).
- Lee, S., and Shum, J. G. (2019). “Prediction of airfoil trailing-edge noise using empirical wall-pressure spectrum models,” *AIAA Journal* **57**(3), 888–897, doi: [10.2514/1.J057787](https://doi.org/10.2514/1.J057787).
- Mascarenhas, D., Cotté, B., and Doaré, O. (2022). “Synthesis of wind turbine trailing edge noise in free field,” *JASA Express Letters* **2**(3), 033601, doi: [10.1121/10.0009658](https://doi.org/10.1121/10.0009658).

Nguyen, P. D., Hansen, K. L., Catcheside, P., Hansen, C. H., and Zajamsek, B. (2021).

“Long-term quantification and characterisation of wind farm noise amplitude modulation,”
Measurement **182**, 109678, doi: [10.1016/j.measurement.2021.109678](https://doi.org/10.1016/j.measurement.2021.109678).

Nyborg, C. M., Bolin, K., Karasalo, I., and Fischer, A. (2023a). “An inter-model comparison
of parabolic equation methods for sound propagation from wind turbines,” Journal of the
Acoustical Society of America **154**(2), 1299–1314, doi: [10.1121/10.0020562](https://doi.org/10.1121/10.0020562).

Nyborg, C. M., Fischer, A., Réthoré, P.-E., and Feng, J. (2023b). “Optimization of wind
farm operation with a noise constraint,” Wind Energy Science **8**(2), 255–276, doi: [10.5194/wes-8-255-2023](https://doi.org/10.5194/wes-8-255-2023).

Ostashev, V. E., Colas, J., Dragna, D., and Wilson, D. K. (2024). “Phase-preserving narrow-
and wide-angle parabolic equations for sound propagation in moving mediaa),” Journal of
the Acoustical Society of America **155**(2), 1086–1102, doi: [10.1121/10.0024460](https://doi.org/10.1121/10.0024460).

Ostashev, V. E., Wilson, D. K., and Muhlestein, M. B. (2020). “Wave and extra-wide-
angle parabolic equations for sound propagation in a moving atmosphere,” Journal of the
Acoustical Society of America **147**(6), 3969–3984, doi: [10.1121/10.0001397](https://doi.org/10.1121/10.0001397).

Scott, J. F., Blanc-Benon, P., and Gainville, O. (2017). “Weakly nonlinear propagation of
small-wavelength, impulsive acoustic waves in a general atmosphere,” Wave Motion **72**,
41–61, doi: [10.1016/j.wavemoti.2016.12.005](https://doi.org/10.1016/j.wavemoti.2016.12.005).

Shen, W. Z., Yunakov, N., Cao, J. F., and Zhu, W. J. (2022). “Development of a general
sound source model for wind farm application,” Renewable Energy **198**, 380–388, doi:
[10.1016/j.renene.2022.07.161](https://doi.org/10.1016/j.renene.2022.07.161).

- Shen, W. Z., Zhu, W. J., Barlas, E., and Li, Y. (2019). “Advanced flow and noise simulation method for wind farm assessment in complex terrain,” *Renewable Energy* **143**, 1812–1825, doi: [10.1016/j.renene.2019.05.140](https://doi.org/10.1016/j.renene.2019.05.140).
- Stevens, R. J. A. M., Graham, J., and Meneveau, C. (2014). “A concurrent precursor inflow method for Large Eddy Simulations and applications to finite length wind farms,” *Renewable Energy* **68**, 46–50, doi: [10.1016/j.renene.2014.01.024](https://doi.org/10.1016/j.renene.2014.01.024).
- Stevens, R. J. A. M., Martínez-Tossas, L. A., and Meneveau, C. (2018). “Comparison of wind farm large eddy simulations using actuator disk and actuator line models with wind tunnel experiments,” *Renewable Energy* **116**, 470–478, doi: [10.1016/j.renene.2017.08.072](https://doi.org/10.1016/j.renene.2017.08.072).
- Sun, Z., Zhu, W., Shen, W., Barlas, E., Sørensen, J., Cao, J., and Yang, H. (2018). “Development of an efficient numerical method for wind turbine flow, sound generation, and propagation under multi-wake conditions,” *Applied Sciences* **9**(1), 100, doi: [10.3390/app9010100](https://doi.org/10.3390/app9010100).
- Tian, Y., and Cotté, B. (2016). “Wind turbine noise modeling based on Amiet’s theory: Effects of wind shear and atmospheric turbulence,” *Acta Acustica united with Acustica* **102**(4), 626–639, doi: [10.3813/AAA.918979](https://doi.org/10.3813/AAA.918979).
- van den Berg, G. P. (2005). “The beat is getting stronger: The effect of atmospheric stability on low frequency modulated sound of wind turbines,” *Noise Notes* **4**(4), 15–40, doi: [10.1260/147547306777009247](https://doi.org/10.1260/147547306777009247).